Original Article

Graded Inconel-stainless steel multi-material structure by inter- and intralayer variation of metal alloys

S.C. Bodner [a,*], K. Hlushko [a], L.T.G. van de Vorst [b], M. Meindlhumer [a], J. Todt [a], M.A. Nielsen [c], J.W. Hooijmans [d], J.J. Saurwalt [d], S. Mirzaei [e,f], J. Keckes [a]

[a] Department of Materials Science, Chair of Materials Physics, Montanuniversität Leoben, A-8700 Leoben, Austria
[b] The Netherlands Organization for Applied Scientific Research TNO — Department Thin Films, 1755-LE Petten, Netherlands
[c] Helmholtz Zentrum Hereon, Institute of Materials Physics, D-21502 Geesthacht, Germany
[d] Admatec Europe BV, 5066 GJ Moergestel, Netherlands
[e] CEITEC BUT, Brno University of Technology, Purkynova 123, CZ- C61200, Czech Republic
[f] Fraunhofer Institute for Material and Beam Technology, Winterbergstraße 28, DE-01277 Dresden, Germany

ARTICLE INFO

ABSTRACT

Additively manufactured multi-metal hybrid structures can be designed as functionally graded materials providing an optimized response at specific positions for particular applications. In this study, *liquid dispersed metal powder bed fusion* is used to synthesize a multi-metal structure based on Inconel 625 (IN625) and stainless steel 316L (S316L) stainless steel regions, built on a S316L base plate. *Both alloys alternate several times along the build direction as well as within the individual sublayers.* The multi-metal sample was investigated by optical microscopy, scanning electron microscopy, microhardness measurements, nano-indentation and energy-dispersive X-ray spectroscopy. Cross-sectional synchrotron X-ray micro-diffraction 2D mapping was carried out at the high-energy material science beamline of the storage ring PETRAIII in Hamburg. Sharp morphological S316L-to-IN625 interfaces along the sample's build direction are observed on the micro- and nanoscale. A gradual phase transition encompassing about 1 mm is revealed in the transverse direction. Mechanical properties change gradually following abrupt or smooth phase transitions between the alloys where a higher strength is determined for the superalloy. The two-dimensional distribution of phases can be assessed indirectly as S316L and IN625 in this multi-metal sample possess a <110> and a <100> fiber crystallographic texture, respectively. Tensile residual stresses of ~900 and ~800 MPa in build direction and perpendicular to it, respectively, are evaluated from measured residual X-ray elastic strains. Generally, the study indicates possibilities and limitations of *liquid dispersed metal powder bed fusion* for additive manufacturing of functionally graded materials with unique synergetic properties and contributes to the understanding of optimization of structurally and functionally advanced composites.

* Corresponding author.
E-mail address: sabine.bodner@unileoben.ac.at (S.C. Bodner).

1. Introduction

Additive manufacturing (AM) of metals is known as a novel production technology that is able to synthesize products of complex geometries for prototyping, mechanical engineering, medicine, automotive and aerospace applications [1]. Contrary to the original assumption that AM could replace a large part of traditional manufacturing processes, the latest developments show that AM will not displace subtractive processes in the future, but rather joins them as a complementary manufacturing technology. The unique advantage of AM technology resides in the ability to customize the shape and size of every individual component. Additionally, relatively recent developments in AM enable to fabricate components with spatially varying functional properties by combining different metals into one functionally graded material (FGM) and/or multi-material hybrid composites [2—5]. FGMs exhibit advantageous functionalities and physical properties, as special requirements like oxidation resistance, thermal strength or toughness can be tailored by optimizing the local use of different materials. In the following, this article refers exclusively to metallic FGMs produced by AM. Their synthetization still poses a particular challenge. This is (i) due to the sometimes very different physical properties of the metals such as the thermal expansion coefficient or the tendency to corrosion, (ii) due to the tendency to form intermetallic phases (depending on the metal combination selected) and (ii) due to the requirements placed on the synthesis process.

The possibility to combine different metal alloys into one workpiece was reported for directed energy deposition (DED) based processes where a layer-wise change or alternation of materials can be realized e.g. by wire arc additive manufacturing (WAAM) and laser metal deposition (LMD) [3,6]. The effort needed for a change of material is manageable using these synthetization methods as only the feedstock (wire or powder) has to be exchanged and fed via a coaxial feeding system to the source of energy [7]. An inherent flexibility is one key point for the production of FGMs. Major drawbacks of DED-based processes are however the limited spatial resolution and surface quality, in particular for small geometries, due to comparably thick layers.

Thus, powder bed fusion (PBF) based processes are regularly used for the production of parts with complex geometries and with higher demands on surface quality and geometric accuracy [4]. If a laser is used as energy source, the correct terminology according to ASTM 52900:2021—11 is laser based powder bed fusion (PBF-LB). Concerning the manufacturing of FGMs, the main drawback of commonly and industrially applied PBF-based processes is the limited flexibility when it comes to a change of the powder feedstock. A spatial variation of materials in state-of-the-art PBF-LB systems means in practice either (i) the application of a printed metal being different from the base plate material [8], (ii) that the whole machine has to be cleaned, before the second (chemically different) powder can be spread over the build area [9] or, (iii) that, if available, a second supplier (cylinder or hopper [10—14]) provides another feedstock and both materials are varied and/or mixed in the build volume. Thus, differentiated process parameters or variations in part's densities (e.g. cellular structures) are rather used than different materials to synthesize FGMs by PBF-LB. Xiong et al. [15] studied mechanical properties of PB-fused TiAl6V4 with density changes due to pores and honeycomb structures which could be considered to be used in orthopedic applications. Ghorbanpour et al. [16] used a commercial available PBF-LB device and influenced the microstructure of the γ''- precipitating Inconel 718 Ni-base alloy by varying the laser powder in different regions along the build direction (BD) and perpendicular to it.

A PBF-LB related process, capable to produce FGMs is liquid dispersed metal powder bed fusion (LDM-PBF-LB). In a previous work [17], the strength and limitations of this relatively novel approach that uses a metal slurry feedstock was indicated. A multi-metal hybrid structure was synthesized, which consisted of five different regions, incorporating both sharp and gradual interfaces between the non-precipitation hardening Ni-base Inconel625 (IN625) alloy and a stainless steel stainless steel 316L (S316L) along the BD. Several transitions of both alloys were realized along the BD. Thus, according to Ref. [2] that sample can be categorized as 2D multi-material structure.

Different approaches to print 2D multi-material structures by PBF-LB were recently studied also by other scientific groups. Mao et al. [18] reported on the influence of process parameters on the formation of the interface in S316 L/CuCrZr FGMs and analyzed corresponding differences of mechanical properties. Chen et al. [19] printed Inconel 718 on a S316 substrate and studied the process-microstructure property relationship in-situ using high-speed synchrotron X-ray imaging. Demir et al. [20] used a prototype PBF-LB system, equipped with a double feeder powder system to fabricate a Fe/Al—12Si multi-material with three distinct regions: pure Fe, Fe/Al12Si blend and Al—12Si.

The variation of a material along a second dimension (*i.e.* within an individual layer) significantly complicates the fabrication of FGMs using PBF-LB techniques. Thus, only a limited number of publications document the successful fabrication of PB-fused 3D multi-metal structures. Wei et al. used a PBF-LB system equipped with six single ultrasonic powder dispensers to produce complex shaped demonstrator parts with discrete and gradual S316 L/Cu10Sn material's variations along the BD and within individual layers. Preliminary results of S316 L/CuSn10 3D multi-metal sample fabricated using a semi-industrial PBF-LB equipment by Aconity 3D and Aerosint were revealed in their collaboration with the ETH Zürich and published in the context of a review on multi-material powder bed fusion techniques by Mehrpouya et al.

[21] The system is equipped with two patterning drums which allows for the simultaneous deposition of up to three materials [22] within an individual layer.

In this work, a 3D multi-metal structure produced by LDM PBF-LB is characterized. S316L and IN625 were alternated twelve times along the BD and more than a hundred times within individual layers (i.e. perpendicular to the BD). An advanced analytical approach aimed at correlating the results of different microscopy methods, energy dispersive spectroscopy (EDS), 2D hardness mapping and cross-sectional synchrotron X-ray micro diffraction (CSmicroXRD). The methods were applied to evaluate the complex microstructure-property-relationship of the fabricated 3D multi-metal sample at different length-scales.

2. Material and methods

Two identical multi-material samples with dimensions of $3 \times 15 \times 7$ mm^3 ($x \times y \times z$) were produced by LDM PBF-LB on a Laserflex Conflux system (Admatec Europe BV, The Netherlands). The system is equipped with a SPI RedPower Laser SP200C (wavelength $\lambda = 1064$ nm) and a galvoscanner-optics, resulting in a small spot size of 12 μm. Gas-atomized Fe and Ni-based powders S316L (size PF-5K by Epson Admix Corp., Japan) and Inconel 625 (Sandvik Osprey, Sweden) with a d_{50} particle size of 4.18 and 3.40 μm, respectively, were mixed with a water-based binder (Admatec Europe BV). The chemical composition was analyzed by EDS in an IntouchScope JSM-6010LA (JEOL, Japan) which was also used for scanning electron microscopy (SEM). Nominal and actual chemical compositions of the used alloys are given in Table 1. Both slurries were selectively applied to the building platform by a pipetting system (Fig. 1b) and spread by a knife edge, resulting in a liquid metal-dispersed powder bed. After a drying step of some seconds, during which the liquid metal-dispersed powder bed densified (Fig. 1b), the metal powders were selectively melted by the laser operated with a power of 137 W (Fig. 1c) in a nitrogen gas atmosphere. The layer thickness, the scan speed, the hatch distance and the alternating angle were set to 20 μm, 500 mm/s, 9 μm and 66°, respectively.

The samples were cleaned from the powder cake and further analyzed by optical microscopy, hardness profiling and CSmicroXRD [17], as described below.

2.1. Metallographic characterization

The specimen (see Fig. 1) was hot-embedded in graphite-filled bakelite "PolyFast" (Struers, Germany). The metallurgical cross-section was prepared by grinding and polishing, finishing with a 1 μm diamond suspension. Two-dimensional phase occurrence at the cross-section was assessed by confocal microscopy using a DCM 3D optical surface metrology system (Leica, Germany) at various magnifications. SEM was carried out on an IntouchScope JSM-6010LA (JEOL, Japan), at voltages of 5 and 15 kV.

2.2. Hardness profiling

Vicker's microhardness measurements were performed across the polished sample cross-section to evaluate hardness gradients at the interfaces between S316L to IN625 in both y and z directions (see Fig. 1). The pyramid-shaped diamond tip was loaded with a test force of 4.905 N, corresponding to HV$_{0.5}$, by a Mitutoyo-Bühler Micromet 5104 hardness-testing device. Distances between two single indents were set to 200 and 500 μm in y and z directions, respectively, and minimum edge-distances were respected according to ASTM E384-99 [23].

2.3. Nanoindentation

Changes in mechanical properties within transition regions between S316L and IN625 were further assessed by a nano-indentation experiment using a Hysitron TI 950 Triboindenter equipped with a Berkovic indenter. The maximum load of 5 mN in the load-controlled regime was employed to prepare arrays of 10 × 10 indents within two sample regions (comprising in-plane- and out-of-plane-oriented interfaces between S316L to IN625). The spacing between two adjacent indents was set to ~50 μm to map the mechanical properties within a larger area. The obtained data were evaluated in terms of hardness and reduced elastic modulus based on the Oliver and Pharr method [24].

2.4. Synchrotron X-ray micro-diffraction

Fig. 2 presents the experimental setup that was used to characterize the specimen by CSmicroXRD at the Hereon operated side-hutch P07B of the high-energy materials science (HEMS) beamline of the storage ring PETRA III at Deutsches Elektronen Synchrotron (DESY) in Hamburg, Germany [25]. The specimen (see Fig. 1a) was scanned along y and z directions using a step size of 50 and 100 μm, respectively, mapping the whole cross-section in transmission diffraction geometry using a beam size of 50 × 100 μm^2 (y × z). The used photon energy of 87.1 keV corresponds to a wavelength of 0.1423 Å.

24.960 diffractograms were collected by a 2D digital X-ray flat panel detector, type XRD1621 (PerkinElmer, Waltham, USA), which has an array size and a pixel pitch of 2048 × 2048

Table 1 – Nominal and actual chemical compositions of S316L and IN625 in ppm (O) and weight.-% (other elements).

S316L	Fe	C	Si	Mn	P	S	Ni	Cr	Mo	O (ppm)
nominal and maximal	Balance	0.03	1.00	<2.00	0.045	0.03	12.0—15.0	16.0—18.0	2.0—3.0	—
Actual	Balance	0.025	0.036	0.11	0.014	0.006	12.14	17.84	2.10	3.400

IN625	Ni	Cr	Mo	Nb	Fe	Al	Co	Ti	Si	Mn
nominal and maximal	Balance	23.0	10.0	4.15	5.0	0.40	1.00	0.40	0.50	0.50
actual	Balance	21.2	9.1	0.24	2.2	0.04	0.01	0.01	0.27	0.24

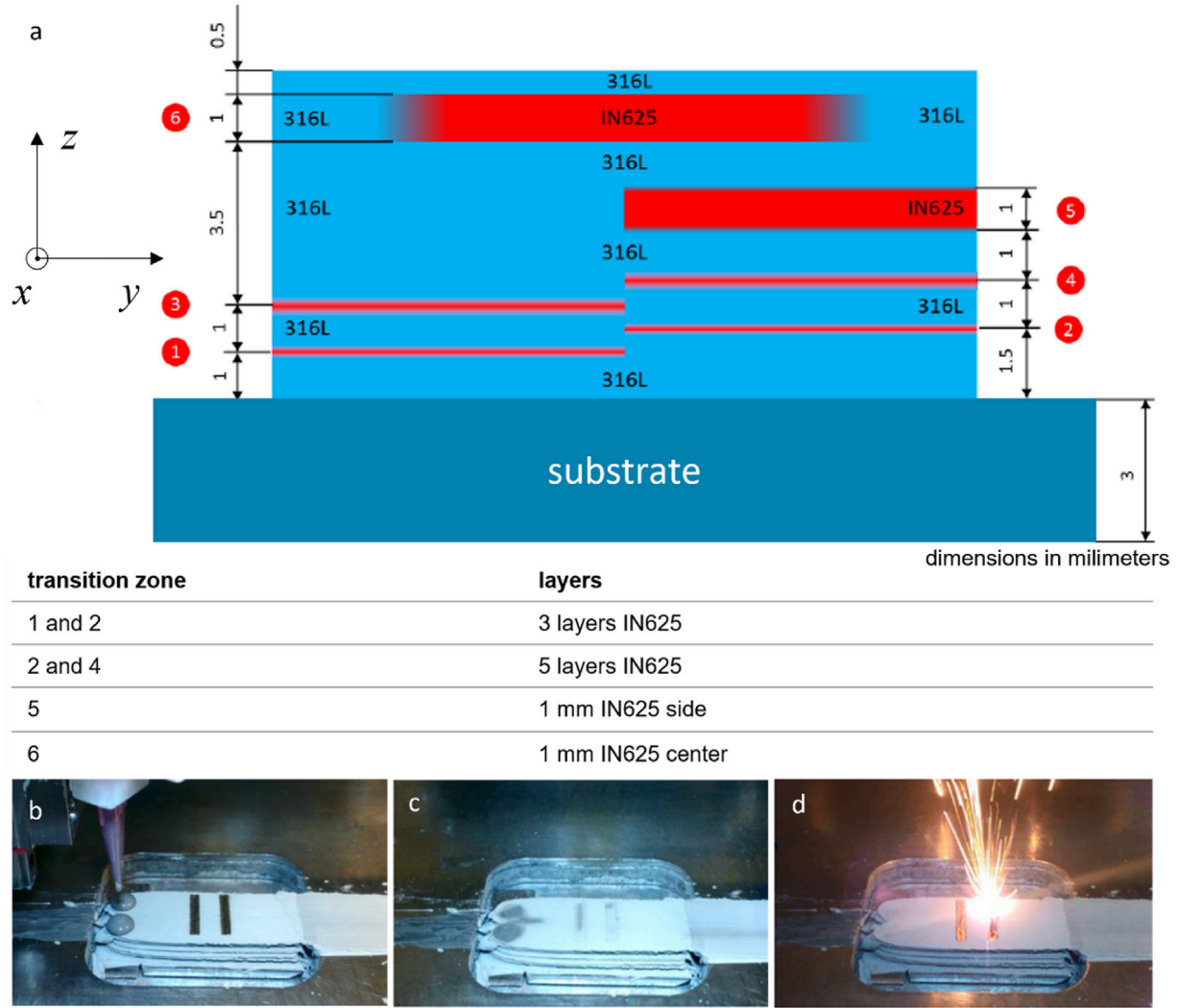| transition zone	layers
1 and 2	3 layers IN625
2 and 4	5 layers IN625
5	1 mm IN625 side
6	1 mm IN625 center

Fig. 1 — Two identical IN625 and S316L multi-material samples (a) were produced by liquid dispersed metal powder bed fusion. The slurries were selectively applied by an automated pipetting system (b), spread across the building platform, resulting in a liquid powder bed and let dry (c) before a laser beam was used to build up the desired geometries layer by layer (d).

pixels and 200 μm, respectively. The sample-to-detector distance, the rotation angle of the tilting plane and the angle of the detector tilt in-plane were calibrated using a LaB_6 standard powder. This methodology named cross-sectional synchrotron X-ray micro-diffraction was introduced in our previous work [17].

3. Theory: residual stress evaluation

2D XRD data were further processed using the python library PyFAI [26] to obtain information on the distribution of phases, microstructure (texture and crystallize size) and strain at the cross-section of the multi-metal sample (averaged along the beam directions) (Fig. 1). Diffraction patterns were azimuthally integrated in the range of $0 < \delta < 360°$, which was split into 36 segments, so-called "cakes", each encompassing a $\Delta\delta$ range of 10°. Lattice parameters $d_{\delta\theta}^{m,hkl}(y,z)$ of (hkl) crystallographic

planes and the particular alloy m were determined from the positions of 311 and the 222 (hkl) reflections using Bragg's law. Each $d_{\delta\theta}^{m,hkl}(y,z)$ value represents the lattice parameter evaluated at the sample position (y,z), while the (hkl) lattice place normal-direction was oriented parallel to the diffraction vector $\mathbf{Q}_{\delta\theta}$ (cf. Fig. 2a).

In the next step, the $d_{\delta\theta}^{m,hkl}(y,z)$ data were used to obtain residual lattice strain $\varepsilon_{\delta\theta}^{m,hkl}(y,z)$ along the direction of the diffraction vector $\mathbf{Q}_{\delta\theta}$ as follows:

$$\varepsilon_{\delta\theta}^{m,hkl}(y,z) = \frac{d_{\delta\theta,}^{m,hkl}(y,z) - d_0^{m,hkl}}{d_{0,m}^{m,hkl}} \tag{1}$$

where δ and θ represent the azimuthal position of the Debye-Scherrer (D-S) rings on the detector (Fig. 2a) and the Bragg's angle, respectively, and $d_0^{m,hkl}$ is the unstressed lattice spacing for the crystallographic plane (hkl).
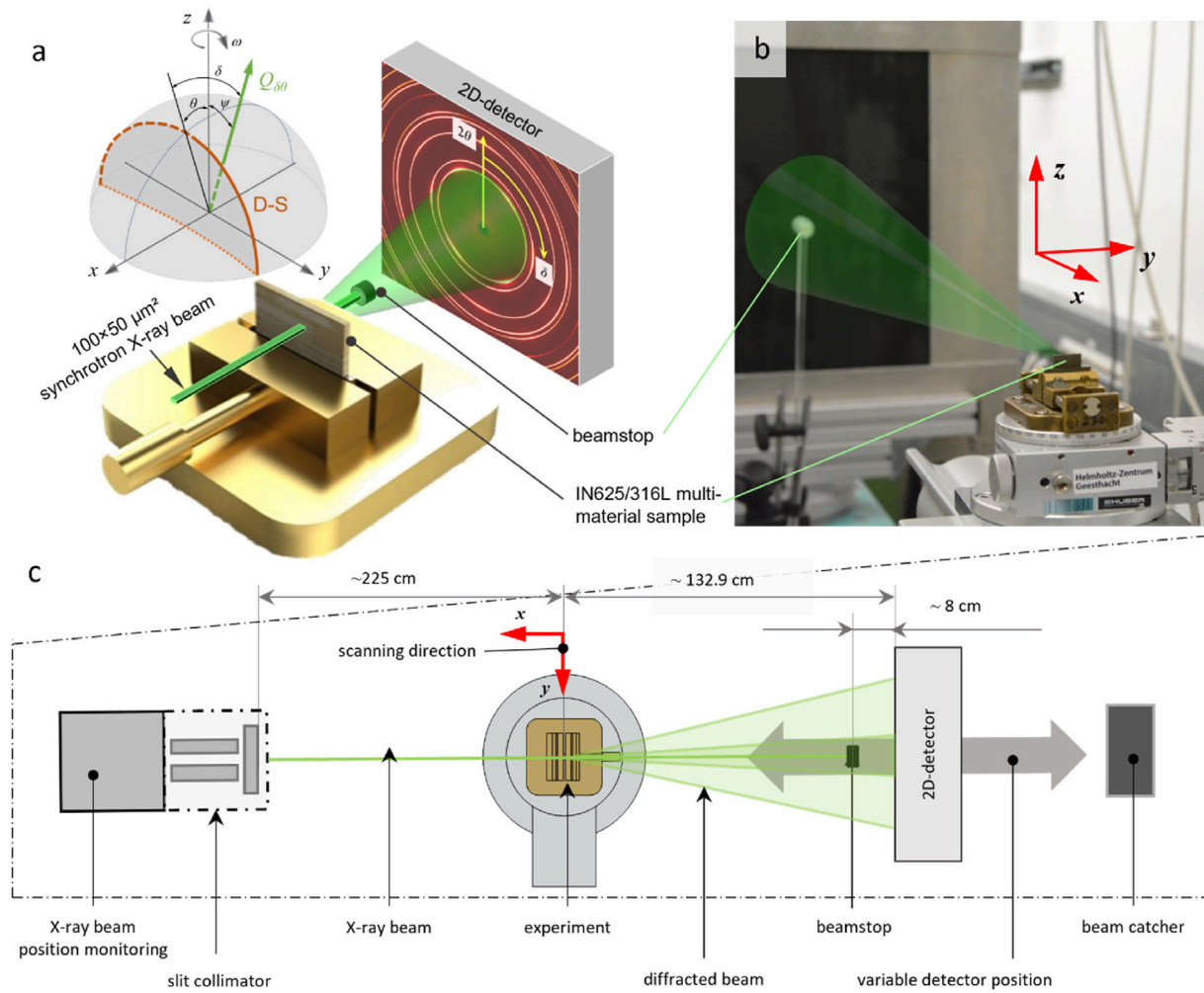
Fig. 2 — Schematic (a, c) and actual (b) experimental setup with indicated X-ray beam and diffraction cone for the cross-sectional X-ray micro-diffraction (CSmicroXRD) [17] measurements at the side-hutch P07B of the HEMS-beamline at PETRA III. The Inconel-steel multi-material sample was mapped in transmission diffraction geometry by scanning the sample in the X-ray beam along y and z axes with increments of 100 and 50 μm, respectively.

A determination of the correct $d_0^{m,hkl}$-values in an additively manufactured multi-metal-material is not trivial, as neither the microstructure nor the chemical composition are homogenous within the sample. In this study, we determined the unstressed lattice parameter a_0^m for both fcc-alloys by fitting the 311 and 222 Debye-Scherrer (D-S) rings for IN625 as well as S316L at several measurement positions located directly next to the free surfaces of the sample, supposing a negligible perpendicular stress component. We obtained a_0^{IN625} and a_0^{316L} of 3.5952 and 3.5948 Å, respectively. These results are in accordance with those determined in [27,28], respectively.

Experimentally determined residual X-ray elastic strains $\varepsilon_{\delta\theta}^{m,hkl}(y,z)$ were used to assess residual stress components $\sigma_{i,j}(y,z);(i,j=x,y,z)$, defined in the sample coordinate system with x, y and z axes, using the following approach:

$$
\begin{aligned}
\varepsilon_{\delta\theta}^{m,hkl}(y,z) = \frac{1}{2}S_2^{m,hkl}\big[&\sin^2\theta\;\sigma_{xx}(y,z) + \cos^2\theta\sin^2\delta\;\sigma_{yy}(y,z) \\
&+ \cos^2\theta\cos^2\delta\;\sigma_{zz}(y,z) + \cos^2\theta\sin 2\delta\;\sigma_{yz}(y,z) \\
&- \sin 2\theta\cos\delta\;\sigma_{xz}(y,z) - \sin 2\theta\sin\delta\;\sigma_{xy}(y,z)\big] \\
+ S_1^{m,hkl}\big[&\sigma_{xx}(y,z) + \sigma_{yy}(y,z) + \sigma_{zz}(y,z)\big]
\end{aligned}
\tag{2}
$$

$S_1^{m,hkl} = \left(-\frac{v}{E}\right)^{hkl}$ and $\frac{1}{2}S_2^{m,hkl} = \left(\frac{1+v}{E}\right)^{hkl}$ are the X-ray elastic constants (XEC) in Voigt's notation. Young's modulus and Poisson's ratio are expressed by E and v, respectively, which are hkl peak-specific due to single crystal anisotropy. Eq. (2) can be derived by applying Hooke's Law for a quasi-isotropic material [29].

The Eshelby-Kroener grain-interaction model [30] was used to calculate XECs, using single-crystal elastic constants of Refs. [31,32], resulting in:

$S_1^{IN625,311} = -1.618 \times 10^{-6}$ MPa^{-1}, $\frac{1}{2}S_2^{IN625,311}$

$= 6.649 \times 10^{-6}$ MPa^{-1}; $S_1^{IN625,222}$

$= -1.108 \times 10^{-6}$ MPa^{-1}, $\frac{1}{2}S_2^{IN625,222}$

$= 5.121 \times 10^{-6}$ MPa^{-1}; $S_1^{316L,311}$

$= -1.378 \times 10^{-6}$ MPa^{-1}, $\frac{1}{2}S_2^{316L,311}$

$= 6.536 \times 10^{-6}$ MPa^{-1}; $S_1^{316L,222}$

$= -0.899 \times 10^{-6}$ MPa^{-1}, $\frac{1}{2}S_2^{316L,222} = 5.098 \times 10^{-6}$ MPa^{-1}

Shear-stress components along planes parallel to the primary X-ray beam (x-direction) were assumed to be negligible ($\sigma_{xy}^m(y, z) \cong 0$; $\sigma_{xz}^m(y, z) \cong 0$. Due to (i) the comparatively small sample dimension in x and (ii) the fact, that the experimental geometry is insensitive to this stress component, calculations within this work are made on the assumption that the corresponding stress component $\sigma_{xx}^m(y, z)$ is zero. Consequently, Eq. (2) can be transformed to

$$\varepsilon_{\delta\theta}^{m,hkl}(y, z) = S_1^{m,hkl}\left[\sigma_{yy}(y, z) + \sigma_{zz}(y, z)\right]$$
$$+ \frac{1}{2}S_2^{m,hkl}\left[\cos^2\theta \sin^2\delta\, \sigma_{yy}(y, z) + \cos^2\theta \cos^2\delta\, \sigma_{zz}(y, z)\right.$$
$$\left. + \cos^2\theta \sin 2\delta\, \sigma_{yz}(y, z)\right]$$

(3)

which allows to determine the stress-state within the investigated area by least-squares fitting of an overdetermined system of 36 equations, based on experimentally determined $\varepsilon_{\delta\theta}^{m,hkl}(y, z)$ [33]. In the following, results of σ_{yy}, σ_{zz} and σ_{yz} are referred to as in-plane, out-of-plane and shear stresses.

3.1. Qualitative phase analysis

Since the steel S316L and IN625 exhibit relatively similar lattice parameters of 3.5948 and 3.5952 Å, respectively, it was not trivial to evaluate the spatial occurrence of both phases from the analysis of D-S rings' intensities. Our former study [17] on a comparable sample indicated that these alloys, printed with similar process parameters, usually possess different crystallographic textures, i.e. a ⟨110⟩ fibre texture for S316L and a ⟨100⟩ fibre texture for IN625. Therefore, in order to qualitatively evaluate the spatial occurrence of the steel S316L and IN625 phases at the sample cross-section, different azimuthal 220 D-S ring intensity maxima within the azimuthal ranges of $350 \le \delta \le 10$ and $35 \le \delta \le 55$ deg were considered, respectively. Hereafter, the spatial occurrence of the steel S316L is presented, where the occurrence of the IN625 phase balances.

3.2. Peak broadening

Changes in diffraction peak widths are influenced by 2nd and 3rd order residual stresses, by gradients of 1st order stresses as well as by the size of coherently scattering domains. In the present case, full-width-at-half-maximum (FWHM) data were used to estimate the size of coherently scattering domains by using a very simplified approach based on the Scherrer equation [34]. For this study, we analyzed the 211_{S316L} and the 311_{IN625} peaks according to Eq. (4) which is a rearrangement of Scherrer's equation by Langford and Wilson [35].

$$p = K \cdot \varepsilon = K \cdot \frac{\lambda}{b \cdot \cos\theta}$$

(4)

where p is the 'true' size of the coherently scattering domains, defined as the cubic root of the crystallite volume. K, ε, λ, b and θ are the Scherrer constant, the apparent crystal size, the wavelength of the used radiation, the additional FWHM-broadening and the Bragg's angle, respectively.

4. Results and discussion

4.1. Cross-sectional microstructure and mechanical properties

The cross-sectional microstructure of the multi-material sample was investigated by confocal laser scanning microscopy, SEM and EDX aiming to determine the distribution of the phases, the individual microstructures and chemical gradients in different regions actually achieved by LDM PBF-LB. The micrographs of the polished cross-section in Fig. 3a and b indicate a clear separation of S316L and IN625 phases (Fig. 3d) *along the BD (further also denoted as the out-of-plane direction)* with morphologically sharp and diffuse interfaces whenever the material changes from S316L to IN625 and from IN625 to S316L, respectively. Remarkably, the latter interface shows an intermixing of the phases with a transition region of ~200 μm. This observation can be attributed to the fact that Ni face-centered crystal structure may solve up to about 50 wt% of alloying elements [36].

Perpendicular to the BD (further also denoted as the in-plane direction), the interface region between the used alloys encompasses a width larger than 1 mm. Furthermore, structural defects due to a lack of binding can be observed here and for the same reason, the occurrence of micro-cracks propagating mainly along high-angle grain boundaries can be observed in625 (Fig. 3c−e). Lack of binding in625 can be addressed to the same origin as the observed higher porosity IN625 region. The occurrence of both, lack of binding as well as a comparatively higher porosity result from the fact, that the process parameters used for both alloys were optimized for processing S316L. The shape of gas pores resulting from excessive energy input is round/spherical. However, the pores present in625 regions of the 3D multi-metal FGM have an irregular, angular shape. Therefore, it can be assumed that these pores were crated by lack of fusion. Their angular surface morphology cause a notch effect and could be identified as the starting point for some high-angle grain boundary cracks. In conclusion, optimized processing of IN625 by LDM PBF-LB would require a higher energy input.

Bundles of oriented, columnar grains, visible in Fig. 3e, originate from the scanning pattern of the laser. Grains grew in the direction of the thermal gradient (z-direction) and their length encompasses several melt pool boundaries. An out-of-plane preferred orientation of these epitaxially grown bundles can be identified in the micrographs. This behaviour has been known for IN625 built by a standard PBF-LB process [37] as well as by other metal AM processes and has also been documented in Ref. [38].
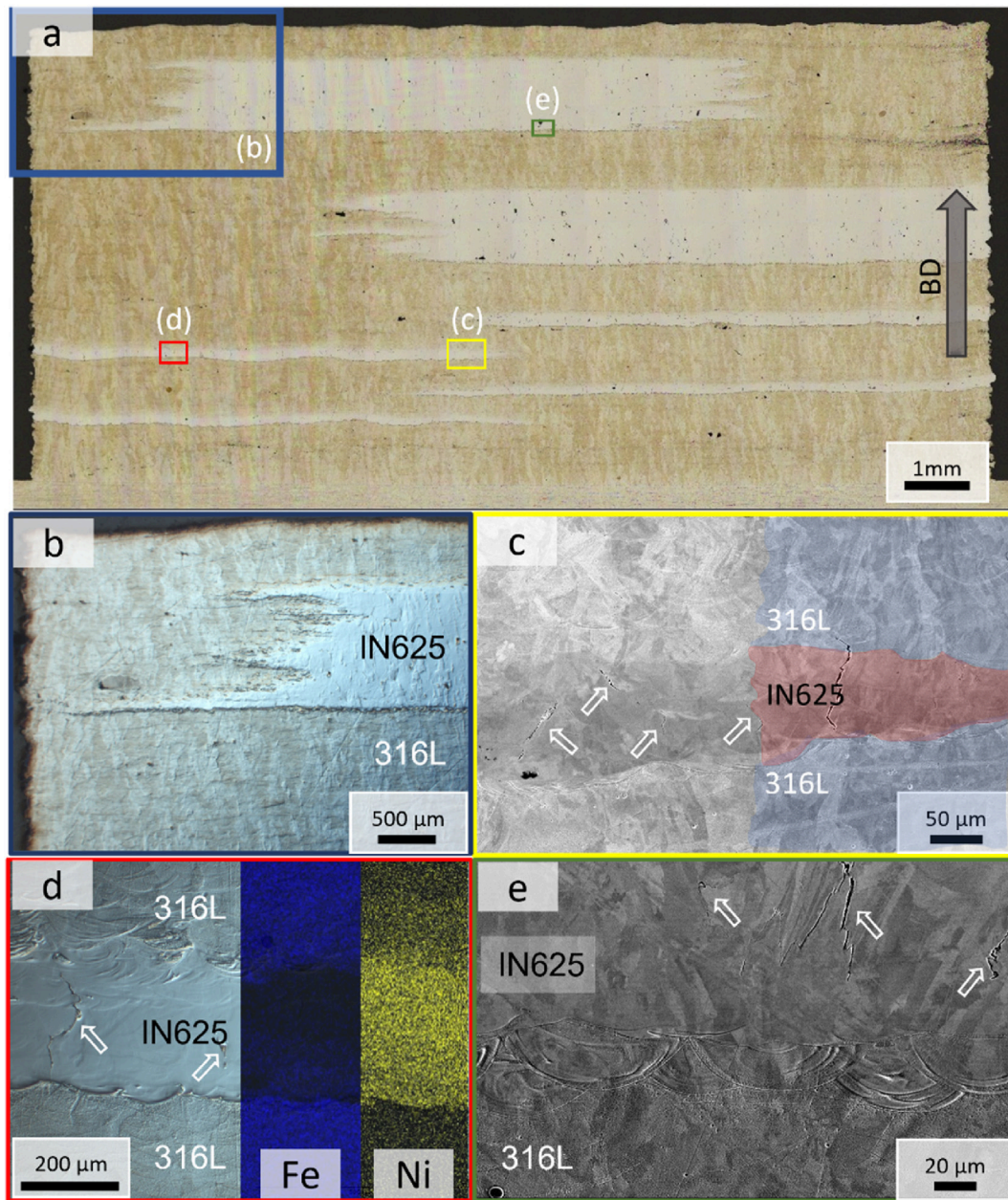
Fig. 3 – Cross-sectional micrographs, recorded using confocal laser scanning microscopy (a,b,d) and SEM (c,e) indicate the presence of micro-cracks in625 regions of the multi-metal sample. Each magnified area from (b) to (d) is highlighted in colour in (a). IN625 regions appear brighter in the overview (a) and the build direction (BD) is indicated by an arrow. An additional chemical analysis by EDS (d) revealed a morphological sharp interface whenever IN625 was applied on S316L but a blurred interface when S316L was applied onto IN625. Perpendicular to the BD, an intermixing at the interface of ~1 mm in width could be determined (b). Bundles of grains with a preferred orientation that correlates with the BD could be determined in the SEM images (c) and (e).

Cahoon et al. [39] indicated that the yield strength of materials can be related to hardness values for brass, steel and aluminium alloys. Thus, Vickers hardness profiling was used to characterize the gradual change of mechanical properties in particular interfacial areas (Fig. 4) Mean microhardness values (H) of 237 ± 5, 285 ± 5 and 168 ± 11 $HV_{0.5}$, corresponding to 2.32 ± 0.05, 2.80 ± 0.05 and 1.65 ± 0.11 GPa were determined

for S316L, IN625 and the S316L base plate, respectively. Measurement points located in the transition area of the two materials were excluded from the evaluation of mean hardness values. Microhardness values in in-plane oriented interface regions change gradually from bulk S316L to IN625 and vice versa within an intermixing zone that encompasses about 2 mm in width (Fig. 4c–d). The gradual change of
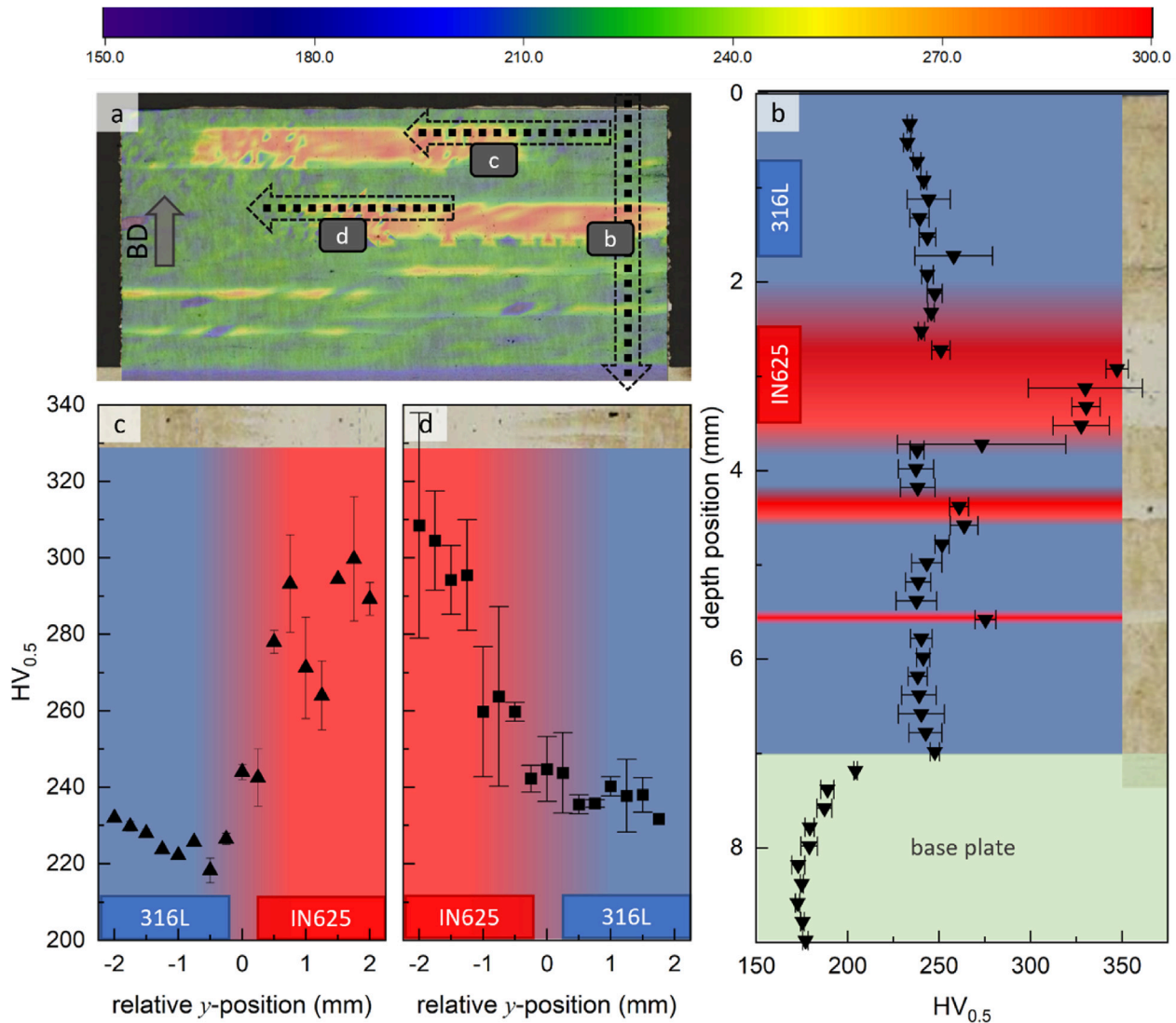
Fig. 4 − Overview optical micrograph with a superimposed 2D hardness chart (a) indicates approximate positions and directions of one vertical (b) and two horizontal (c,d) microhardness scans used to determine Vickers hardness across the S316L and IN625 interfaces. Error bars for each measurement position represent the standard deviation calculated from three measurement points at comparable spatial positions.

microhardness values correlates to the width of the inter-mixing zone in which the chemical composition of both alloys change gradually from S316L to IN625.

Due to the higher spatial resolution needed in order to determine local mechanical properties nanoindentation mapping in an area of 500×500 μm^2 at the top of the region 5 (cf. Fig. 5) was conducted. Reduced moduli for S316L and IN625 were measured using nanoindentation and evaluated to be ~181 and ~191 GPa, respectively. Nanohardness values ($H_{O−P}$), determined by the Oliver-Pharr method [24], increased from ~3.4 ± 0.1 GPa in S316L to ~4.7 ± 0.1 GPa in625. These values are obviously higher than the values determined by the micro-hardness measurements.

Even though the processing route of the multi-material sample investigated in this study differs from a standard PBF-LB process in industry (previously also known as laser melting process) [40−42], the determined hardness values for the S316L alloy can be compared with literature results [43] but are about ~7% higher than the macro-hardness value of ~221 HV_{10} reported in Refs. [44,45]. Valente et al. [46] investigated the influence of different protective gas atmospheres used in PBF-LB and observed systematically higher hardness values for samples built in an N_2 atmosphere which was also the case in the present study. The authors explained their observation with a remarkable solubility of N in stainless steel while Ar as an inert gas is not soluble.

The determined hardness values of 285 ± 5 $HV_{0.5}$ for IN625 were compared with results of macro- and microhardness measurements published in data sheets and literature [37,47−49]. SLM Solutions [47] provides slightly varying values of 291−310 HV_{10} for the as-built condition, depending on the layer thickness that was used in their process. The reported tendency suggests that material's hardness decreases with an increasing layer thickness. Wong et al. [38] documented the
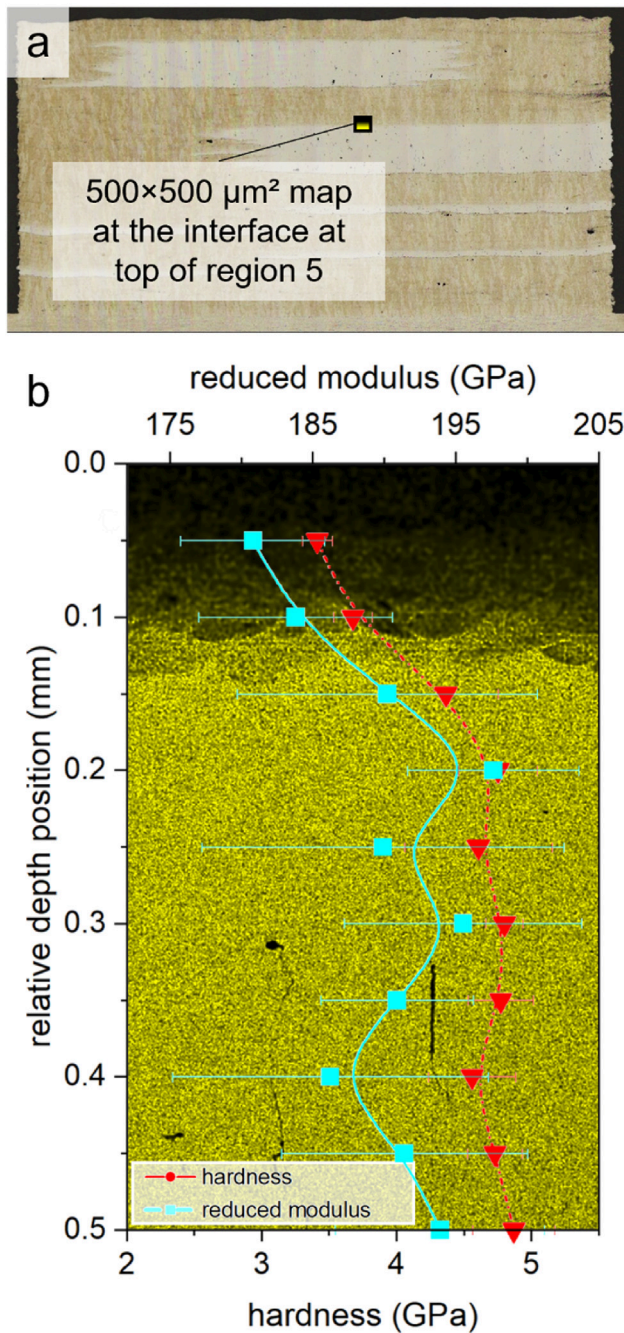
Fig. 5 – Local mechanical properties (hardness and reduced modulus) at the S316 L/IN625 interface were determined by nanoindentation. Indentation was performed in a 500 × 500 μm large region which is marked in (a). The profiles of hardness and reduced modulus are shown across the SEM-EDX map of Ni in (b). Error bars for each measurement position represent the standard deviation calculated from ten indents at comparable spatial positions.

dependence of hardness values on badly/well optimized parameters used during a multi-laser PBF-LB process. It can be concluded that the values reported here are in good accordance with results of (micro) hardness measurements on samples synthesized by standard PBF-LB processes.

A gradual adaptation in transition zones, comparable to the in-plane and out-of-plane oriented intermixing zones of this sample, has also been determined in the case of a S316 L/Cu10Sn multi-metal system [50] as well as for a S316 L/C184000 (Cu alloy) material combination [51].

A similar behaviour was observed by Qian et al. [52] for five inorganic materials, including Cu and stainless steel 304. The authors report nanoindentation hardness to be 10−30% higher compared to microhardness. The deviation of results is explained with respect to differences in the applied methods. In the case of nanoindentation, hardness values are evaluated using the projected contact area at the full load, while in the case of microhardness experiments, values are post-experimentally determined from the residual projected area. Further deviations between the methods stem from indentation-size effects, among these are (i) disproportionately larger influences of pile-ups [24], (ii) dislocation density [53], (iii) volume deformation energy and (iv) free surface energy [54]. In the present work, ratios of $H_{O−P}/H$ were calculated to be 0.68 and 0.60 for S316L and IN625, respectively. Thus, the deviation between nano- and microhardness values was found to be larger than in Ref. [52] where the experimental determined $H_{O−P}/H$ ratio for stainless steel 304 was determined to be 0.73. A possible explanation for the even larger deviation in the case of IN625 are microcracks and pores in the respective region. In nanoindentation experiments, the surrounding region that provides support for the plastically deformed area during indentation is relatively smaller than in microhardness testing. Consequently, with the increasing penetration depth and size of the indent, the probability increases that pores or microcracks are present in the surrounding region during microhardness measurements. Their influence results in lower experimentally determined hardness values.

4.2. Residual stress distribution, texture and microstructure

CSmicroXRD was performed to assess the distribution of the stress state, the texture, phases and microstructural changes in the build up. The information was derived from 2D diffractograms which were used to quantify the residual strain state in the synthesized multi-material sample. In a next step, the residual stress distribution was calculated (Sec. 3) by using the corresponding XECs of both materials. As the XECs of the materials are different, residual stresses in625 and S316L were calculated separately. In-plane, out-of-plane and shear stresses, are illustrated in Figs. 6 and 7a, b and c, respectively. The distribution of residual stresses in Figs. 6 and 7 correlates well with stress-formation models of Ref. [55] and helps to understand mechanisms affecting the crack initiation in AM materials. The in-plane stress distribution in Fig. 7a in the uppermost layers shows maximal tensile stresses of approx. 400 MPa in the specimen's centre and reduced tensile stresses of approx. 50 MPa or nearly stress-free regions at the left and right edges of the specimen. As indicated in Figs. 6c and 7c, shear stresses in the respective area are negligible. In-plane residual stresses (Figs. 6a and 7a) in the topmost layer are thus relevant especially for solidification cracking and crack propagation parallel to the BD, which is the z-direction in this
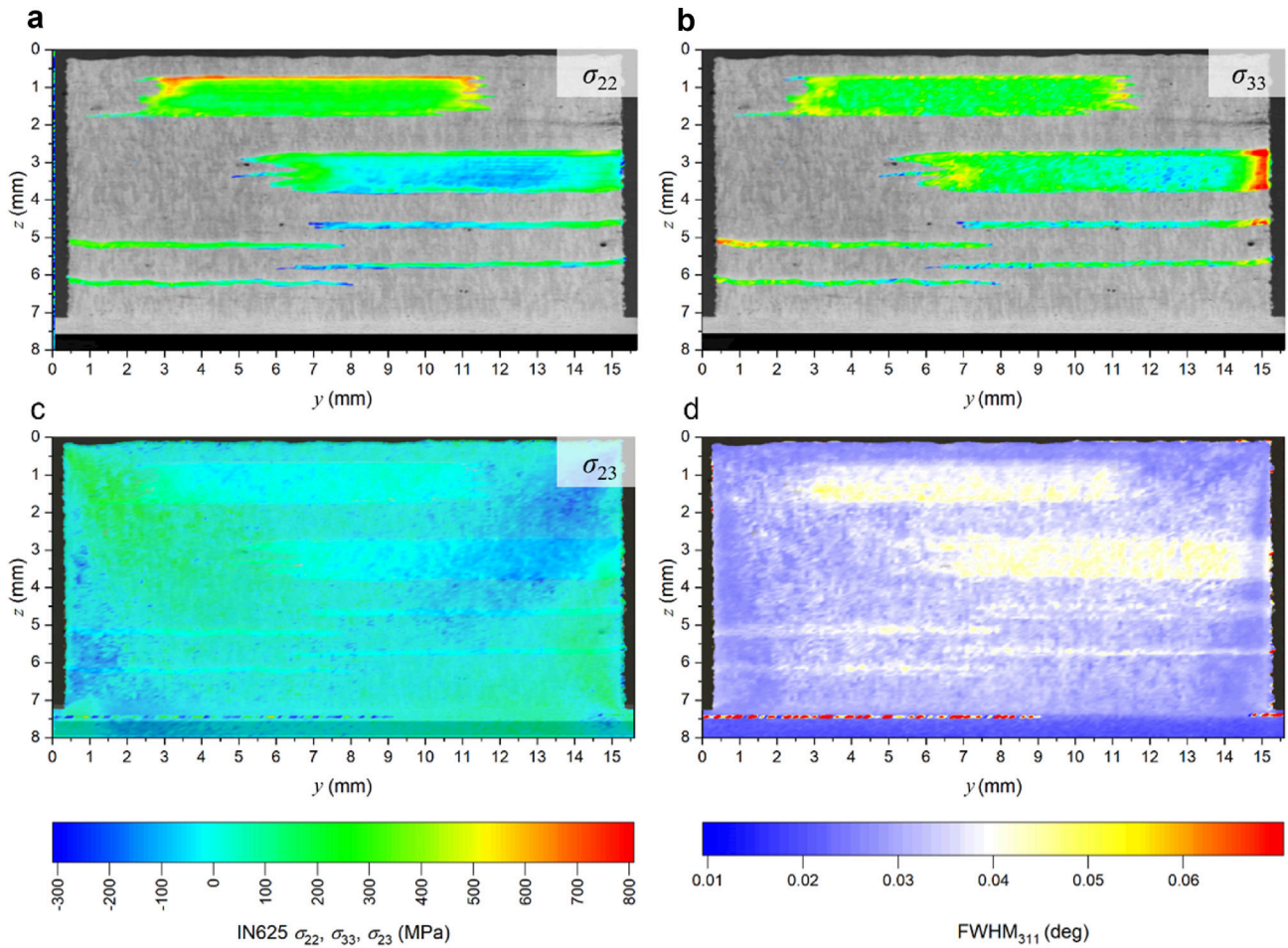
Fig. 6 — Stack of the optical micrographs of S316L and the 2D residual stress distributions in625. Residual stresses were calculated from the residual strain distribution in the sample for in-plane normal stresses (a), out-of-plane normal stresses (b) and shear stresses in (c). FWHM values of the 311 peak (d) indicate coarser grains in S316L compared to the brighter appearing areas of IN625.

case. At greater depths of >1 mm, in-plane residual stresses behave in the opposite way, exhibiting a (compressive) minimum in the sample's centre and moderate (tensile) maxima at the left and right edges.

Furthermore the evaluation of experimental data exhibited stress concentrations in both phases whenever the printed material changed from IN625 to S316L. Maximal tensile stresses of approx. 800 MPa could be detected on top of sample region 6 due to the superposition of (i) the stress component given by the temperature gradient mechanism [56] and (ii) the stress component induced during the cool-down phase of the molten top layers.

In contrast, stresses in the out-of-plane orientation were determined to reach maximal levels of >900 MPa at the left and right edges of the specimen (Figs. 6(b) and 7(b)). Like the distribution of in-plane residual stresses, this correlates well with predicted results from simulations [55] and helps to understand the strong tendency for crack propagation perpendicular to the BD, starting at the sample's edges. This kind of crack propagation is often referred to as "delamination" and can be found in various PBF-LB materials [57—59]. It is important to notice that the evaluated stress levels

correspond to stress components of the Cauchy stress tensor. These components can thus exceed the yield strength of the materials as the yield strength determined in uniaxial tensile tests does not represent the stress components but the yield criterion described e.g. by the maximum energy distortion criterion.

Being aware of the fact, that the broadening of XRD peaks is influenced by micro strains, structural defects, temperature factors, stress gradients and the instrumental broadening, the FWHM data from Fig. 6a were used to qualitatively estimate the size of coherently scattering domains across the specimen [35]. According to Scherrer's formula [34], a qualitative interpretation of the FWHM map thus suggests a smaller crystallite size in the IN625 areas compared to S316L.

Beside the crystallite size, also the spatial occurrence of the phases was evaluated from the D-S rings by considering the $\langle 110 \rangle$ and $\langle 100 \rangle$ fibre textures of S316L and IN625 phases. These two types of textures were identified already in our previous publication. Fig. 7d shows the spatial occurrence of S316L phase, where the IN625 is given by the balance.

The phase analysis did not exhibit the formation of intermetallic compounds at interface regions of the S316 L/IN625
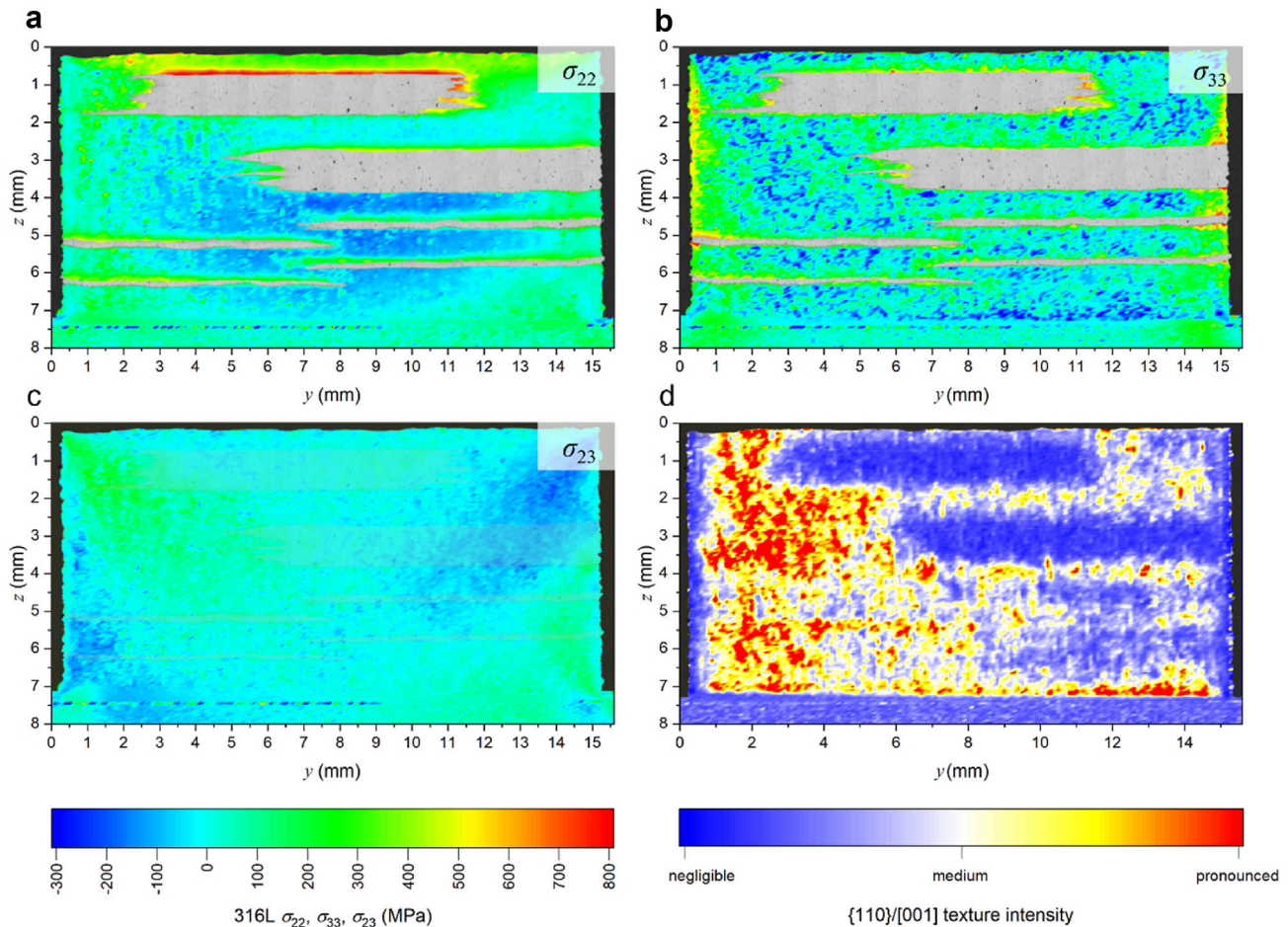
Fig. 7 – Stack of the optical micrograph of IN625 and the 2D residual stress distribution in S316L. Residual stresses were calculated from the residual strain distribution in the sample for in-plane normal stresses (a), out-of-plane normal stresses (b) and shear stresses in (c). The qualitative evaluation of crystallographic texture (d) in the sample indicates a pronounced ⟨110⟩ texture in S316L. It has been known from a previous study that IN625 has a preferential orientation of the ⟨100⟩-lattice directions parallel to the BD.

material. The intermixing of both alloys was studied intensively in a previous work [17].

5.   Conclusions

The present work documents the application of correlative standard and advanced characterization methods to investigate the complex microstructure, mechanical properties and the distribution of residual stresses in a printed 3D multi-metal FGM. Two identical specimens were synthesized by LDM PBF-LB which represents a relatively novel technique based on the use of slurries instead of powders in a PBF-LB process. The samples' cross-sections were subjected to micro- and nanohardness tests and furthermore characterized by confocal microscopy and SEM, EDS and CSmicroXRD. Results of this study indicated that:

- Stainless steel S316L and IN625 were successfully combined layer-by-layer (in build-direction z) and within individual sub-layers (x-y direction) with resolutions better

than 200 μm and of about 1 mm, respectively, to form solid 3D multi-metal FGMs.
- Nanohardness experiments revealed a gradual change of mechanical properties at interface regions of the build-up. Microhardness gradually changed from 237 ± 5 in the stainless steel to 285 ± 5 $HV_{0.5}$ in the Ni-base alloy at graded horizontal and morphological sharp vertical interfaces.
- Reduced moduli of ~181 and ~191 GPa for S316L and IN625, respectively, of the pure alloys and at one interface were assessed by nanoindentation mapping.
- CSmicroXRD mapping indicated the presence of significant residual stresses of approx. 800 MPa in the in-plane direction (i.e. the y-direction, oriented perpendicular to the BD). Maximal residual stresses of >900 MPa were determined in out-of-plane orientation (i.e. the z-direction, oriented parallel to the BD). Shear components in these build-ups could be neglected due to their negligible degree of expression.

The experimentally assessed results of this work lead to a deeper understanding of an optimized design of multi-metal

3D FGMs synthesized by PBF-LB related AM technologies in terms of crack-initiation and crack-propagation.

Author's contribution statement

Declaration of Competing Interest

The authors declare that they have no known competing financial interests or personal relationships that could have appeared to influence the work reported in this paper.

Acknowledgements

REFERENCES

[1] Li C, Liu ZY, Fang XY, Guo YB. Residual stress in metal additive manufacturing. Procedia CIRP 2018;71:348−53. https://doi.org/10.1016/J.PROCIR.2018.05.039.

[2] Schneck M, Horn M, Schmitt M, Seidel C, Schlick G, Reinhart G. Review on additive hybrid- and multi-material-manufacturing of metals by powder bed fusion: state of technology and development potential. Prog in Addit Manuf 2021;6:881−94. https://doi.org/10.1007/s40964-021-00205-2.

[3] Li Y, Feng Z, Hao L, Huang L, Xin C, Wang Y, et al. A review on functionally graded materials and structures via additive manufacturing: from multi-scale design to versatile functional properties. Adv Mater Technol 2020;5. https://doi.org/10.1002/admt.201900981.

[4] Ghanavati R, Naffakh-Moosavy H. Additive manufacturing of functionally graded metallic materials: a review of experimental and numerical studies. J Mater Res Technol 2021;13:1628−64. https://doi.org/10.1016/j.jmrt.2021.05.022.

[5] Balla VK, DeVasConCellos PD, Xue W, Bose S, Bandyopadhyay A. Fabrication of compositionally and structurally graded Ti−TiO2 structures using laser engineered net shaping (LENS). Acta Biomater 2009;5:1831−7. https://doi.org/10.1016/j.actbio.2009.01.011.

[6] Carroll BE, Otis RA, Borgonia JP, Suh J, Dillon RP, Shapiro AA, et al. Functionally graded material of 304L stainless steel and inconel 625 fabricated by directed energy deposition: characterization and thermodynamic modeling. Acta Mater 2016;108:46−54. https://doi.org/10.1016/J.ACTAMAT.2016.02.019.

[7] Schneck M, Horn M, Schindler M, Seidel C. Capability of multi-material laser-based powder bed fusion—development and analysis of a prototype large bore engine component. Metals 2022;12. https://doi.org/10.3390/met12010044.

[8] Fox P, Pogson S, Sutcliffe CJ, Jones E. Interface interactions between porous titanium/tantalum coatings, produced by Selective Laser Melting (SLM), on a cobalt-chromium alloy. Surf Coating Technol 2008;202:5001−7. https://doi.org/10.1016/j.surfcoat.2008.05.003.

[9] Borisov E, Polozov I, Starikov K, Popovich A, Sufiiarov V. Structure and properties of Ti/Ti64 graded material manufactured by laser powder bed fusion. Materials 2021;14. https://doi.org/10.3390/ma14206140.

[10] Wei C, Sun Z, Chen Q, Liu Z, Li L. Additive manufacturing of horizontal and 3D functionally graded 316L/Cu10Sn components via multiple material selective laser melting. J of Manuf Sci and Eng, Trans of the ASME 2019;141:1−8. https://doi.org/10.1115/1.4043983.

[11] Wei C, Gu H, Li Q, Sun Z, hui Chueh Y, Liu Z, et al. Understanding of process and material behaviours in additive manufacturing of Invar36/Cu10Sn multiple material components via laser-based powder bed fusion. Addit Manuf 2021;37:101683. https://doi.org/10.1016/j.addma.2020.101683.

[12] Wang D, Deng GW, qiang Yang Y, Chen J, hui Wu W, liang Wang H, et al. Interfacial microstructure and mechanical properties of selective laser melted multilayer functionally graded materials. J Cent S Univ 2021;28:1155−69. https://doi.org/10.1007/s11771-021-4687-9.

[13] Beal VE, Erasenthiran P, Ahrens CH, Dickens P. Evaluating the use of functionally graded materials inserts produced by selective laser melting on the injection moulding of plastics parts. Proc IME B J Eng Manufact 2007;221:945−54. https://doi.org/10.1243/09544054JEM764.

[14] Nadimpalli VK, Hørdum E, Dahmen T, Valente EH, Mohanty S. Multi-material additive manufacturing of steels using laser powder bed fusion eu spen ' s 1 9 th International Conference & Exhibition , Bilbao , ES. June 2019. Multi-material additive manufacturing of steels using laser powder bed fusion 2019.

[15] Xiong YZ, Gao RN, Zhang H, Dong LL, Li JT, Li X. Rationally designed functionally graded porous Ti6Al4V scaffolds with high strength and toughness built via selective laser melting for load-bearing orthopedic applications. J Mech Behav Biomed Mater 2020;104:103673. https://doi.org/10.1016/j.jmbbm.2020.103673.

[16] Ghorbanpour S, Deshmukh K, Sahu S, Riemslag T, Reinton E, Borisov E, et al. Additive manufacturing of functionally graded inconel 718: effect of heat treatment and building orientation on microstructure and fatigue behaviour. J Mater Process Technol 2022;306:117573. https://doi.org/10.1016/j.jmatprotec.2022.117573.

[17] Bodner SC, van de Vorst LTG, Zalesak J, Todt J, Keckes JF, Maier-Kiener V, et al. Inconel-steel multilayers by liquid dispersed metal powder bed fusion: microstructure, residual stress and property gradients. Addit Manuf 2020;32. https://doi.org/10.1016/j.addma.2019.101027.

[18] Mao S, Zhang DZ, Ren Z, Fu G, Ma X. Effects of process parameters on interfacial characterization and mechanical properties of 316L/CuCrZr functionally graded material by selective laser melting. J Alloys Compd 2022;899:163256. https://doi.org/10.1016/j.jallcom.2021.163256.

[19] Chen WY, Zhang X, Li M, Xu R, Zhao C, Sun T. Laser powder bed fusion of Inconel 718 on 316 stainless steel. Addit Manuf 2020;36:101500. https://doi.org/10.1016/j.addma.2020.101500.

[20] Demir AG, Previtali B. Multi-material selective laser melting of Fe/Al-12Si components. Manuf Lett 2017;11:8–11. https://doi.org/10.1016/j.mfglet.2017.01.002.

[21] Mehrpouya M, Tuma D, Vaneker T, Afrasiabi M, Bambach M, Gibson I. Multimaterial powder bed fusion techniques. Rapid Prototyp J 2022;28:1–19. https://doi.org/10.1108/RPJ-01-2022-0014.

[22] Aerosint. Multi-material 3D printing bundle for laser powder bed fusion. 2020. https://aerosint.com/multi-material-3d-printing-bundle. [Accessed 3 November 2022].

[23] ASTM International. Standard test method for microindentation hardness of materials. ASTM International; 2016.

[24] Oliver WC, Pharr GM. An improved technique for determining hardness and elastic modulus using load and displacement sensing indentation experiments. J Mater Res 1992;7:1564–83. https://doi.org/10.1557/JMR.1992.1564.

[25] Schell N, King A, Beckmann F, Fischer T, Müller M, Schreyer A. The high energy materials science beamline (HEMS) at PETRA III. Mater Sci Forum 2014;772:57–61. https://doi.org/10.4028/www.scientific.net/MSF.772.57.

[26] Kieffer J, Karkoulis D. PyFAI, a versatile library for azimuthal regrouping. J Phys Conf 2013;425. https://doi.org/10.1088/1742-6596/425/20/202012.

[27] Rai SK, Kumar A, Shankar V, Jayakumar T, Bhanu Sankara Rao K, Raj B. Characterization of microstructures in Inconel 625 using X-ray diffraction peak broadening and lattice parameter measurements. Scripta Mater 2004;51:59–63. https://doi.org/10.1016/j.scriptamat.2004.03.017.

[28] Bacci T, Borgioli F, Galvanetto E, Pradelli G. Glow-discharge nitriding of sintered stainless steels. Surf Coating Technol 2001;139:251–6. https://doi.org/10.1016/S0257-8972(01)01010-6.

[29] Welzel U, Ligot J, Lamparter P, Vermeulen AC, Mittemeijer EJ. Stress analysis of polycrystalline thin films and surface regions by X-ray diffraction. J Appl Crystallogr 2005;38:1–29. https://doi.org/10.1107/S0021889804029516.

[30] Kröner E. Berechnung der elastischen Konstanten des Vielkristalls aus den Konstanten des Einkristalls. Z Phys 1958;151:504–18. https://doi.org/10.1007/BF01337948.

[31] Wang Z, Stoica AD, Ma D, Beese AM. Diffraction and single-crystal elastic constants of Inconel 625 at room and elevated temperatures determined by neutron diffraction. Mater Sci Eng 2016;674. https://doi.org/10.1016/j.msea.2016.08.010.

[32] Noyan Ismail C, Cohen Jerome B. Residual Stress – Measurment by Diffraction and Interpretaion. In: Materials Research and Engineering. New York, NY: Springer; 1987. p. 35. https://doi.org/10.1007/978-1-4613-9570-6.

[33] Zeilinger A, Todt J, Krywka C, Müller M, Ecker W, Sartory B, et al. In-situ observation of cross-sectional microstructural changes and stress distributions in fracturing TiN thin film during nanoindentation. Sci Rep 2016;6. https://doi.org/10.1038/srep22670.

[34] Scherrer P. Bestimmung der Größe und der inneren Struktur von Kolloidteilchen mittels Röntgenstrahlen. Nachrichten von Der Gesellschaft Der Wissenschaften Zu Göttingen. Math-Phys Kl 1918;2:98–100. https://doi.org/10.1007/978-3-662-33915-2.

[35] Langford JI, Wilson AJC. Scherrer after sixty years: a survey and some new results in the determination of crystallite size. J Appl Crystallogr 1978;11:102–13. https://doi.org/10.1107/S0021889878012844.

[36] Sravan Sashank S, Rajakumar S, Karthikeyan R, Nagaraju DS. Weldability, mechanical properties and microstructure of nickel based super alloys: a review. E3S Web of Conferences 2020;184:1–6. https://doi.org/10.1051/e3sconf/202018401040.

[37] Gamon A, Arrieta E, Gradl PR, Katsarelis C, Murr LE, Wicker RB, et al. Microstructure and hardness comparison of as-built inconel 625 alloy following various additive manufacturing processes. Results in Materials 2021;12:100239. https://doi.org/10.1016/j.rinma.2021.100239.

[38] Wong H, Dawson K, Ravi GA, Howlett L, Jones RO, Sutcliffe CJ. Multi-laser powder bed fusion benchmarking—initial trials with inconel 625. Int J Adv Manuf Technol 2019;105:2891–906. https://doi.org/10.1007/s00170-019-04417-3.

[39] Cahoon JR, Broughton WH, Kutzak AR. The determination of yield strength from hardness measurements. Metall Trans A 1971;2:1979. https://doi.org/10.1007/BF02913433. –83.

[40] Gu DD, Meiners W, Wissenbach K, Poprawe R. Laser additive manufacturing of metallic components: materials, processes and mechanisms. Int Mater Rev 2012;57:133–64. https://doi.org/10.1179/1743280411Y.0000000014.

[41] Singh R, Gupta A, Tripathi O, Srivastava S, Singh B, Awasthi A, et al. Powder bed fusion process in additive manufacturing: an overview. Mater Today Proc 2019;26:3058–70. https://doi.org/10.1016/j.matpr.2020.02.635.

[42] Bhavar V, Kattire P, Patil V, Khot S, Gujar K, Singh R. A review on powder bed fusion technology of metal additive manufacturing. Additive Manufacturing Handbook: Product Development for the Defense Industry 2017;251–61. https://doi.org/10.1201/9781315119106.

[43] Liverani E, Toschi S, Ceschini L, Fortunato A. Effect of selective laser melting (SLM) process parameters on microstructure and mechanical properties of 316L austenitic stainless steel. J Mater Process Technol 2017;249:255–63. https://doi.org/10.1016/j.jmatprotec.2017.05.042.

[44] Slm Solutions Group AG. Materialdatenblatt Fe-Alloy 316L (1.4404) n.d.:4–8.

[45] Oerlikon AM. Additive manufacturing of 316L stainless steel. Int J Recent Technol Eng 2019;8:6825–9. https://doi.org/10.35940/ijrte.d5199.118419.

[46] Valente EH, Nadimpalli VK, Andersen SA, Pedersen DB, Christiansen TL, Somers MAJ. Influence of atmosphere on microstructure and nitrogen content in AISI 316L fabricated by laser-based powder bed fusion. European Society for Precision Engineering and Nanotechnology, Conference Proceedings - 19th International Conference and Exhibition, EUSPEN 2019 2019:244–7.

[47] Slm Solutions Group AG. Material data sheet Ni-alloy IN625/2.4856/B446 2016:2–6.

[48] EOS GmbH. Material data sheet Technical data 2015;49:1–6. IN625.

[49] Wong KV, Hernandez A. A review of additive manufacturing. ISRN Mechanical Engineering 2012;2012:1–10. https://doi.org/10.5402/2012/208760.

[50] Chen J, Yang Y, Song C, Zhang M, Wu S, Wang D. Interfacial microstructure and mechanical properties of 316L/CuSn10 multi-material bimetallic structure fabricated by selective laser melting. Mater Sci Eng 2019;752:75—85. https://doi.org/10.1016/j.msea.2019.02.097.

[51] Liu ZH, Zhang DQ, Sing SL, Chua CK, Loh LE. Interfacial characterization of SLM parts in multi-material processing: metallurgical diffusion between 316L stainless steel and C18400 copper alloy. Mater Char 2014;94:116—25. https://doi.org/10.1016/j.matchar.2014.05.001.

[52] Qian L, Li M, Zhou Z, Yang H, Shi X. Comparison of nano-indentation hardness to microhardness. Surf Coating Technol 2005;195:264—71. https://doi.org/10.1016/j.surfcoat.2004.07.108.

[53] Nix WD, Gao H. Indentation size effects in crystalline materials: a law for strain gradient plasticity. J Mech Phys Solid 1998;46:411—25. https://doi.org/10.1016/S0022-5096(97)00086-0.

[54] Fröhlich F, Grau P, Grellmann W. Performance and analysis of recording microhardness tests. Phys Status Solidi 1977;42:79—89. https://doi.org/10.1002/pssa.2210420106.

[55] Mercelis P, Kruth J. Residual stresses in selective laser sintering and selective laser melting. Rapid Prototyp J 2006;12:254—65. https://doi.org/10.1108/13552540610707013.

[56] Megahed M, Mindt HW, N'Dri N, Duan H, Desmaison O. Metal additive-manufacturing process and residual stress modeling, vol. 5. Integrating Materials and Manufacturing Innovation; 2016. https://doi.org/10.1186/s40192-016-0047-2.

[57] Platl J, Bodner S, Hofer C, Landefeld A, Leitner H, Turk C, et al. Cracking mechanism in a laser powder bed fused cold-work tool steel: the role of residual stresses, microstructure and local elemental concentrations. Acta Mater 2022;225:117570. https://doi.org/10.1016/j.actamat.2021.117570.

[58] Mohr G, Altenburg SJ, Ulbricht A, Heinrich P, Baum D, Maierhofer C, et al. In-situ defect detection in laser powder bed fusion by using thermography and optical tomography—comparison to computed tomography. Metals 2020;10. https://doi.org/10.3390/met10010103.

[59] Kempen K, Vrancken B, Buls S, Thijs L, Van Humbeeck J, Kruth JP. Selective laser melting of crack-free high density M2 high speed steel parts by baseplate preheating. Journal of Manufacturing Science and Engineering, Transactions of the ASME 2014;136. https://doi.org/10.1115/1.4028513.